

Thermal conductivity of bottle-brush polymers

Manoj Kumar Maurya,¹ Tobias Laschuetza,^{2,3} Manjesh Kumar Singh,^{1,*} and Debashish Mukherji^{3,†}

¹*Department of Mechanical Engineering, Indian Institute of Technology Kanpur, Kanpur UP 208016 India*

²*Institute of Mechanics, Karlsruhe Institute of Technology (KIT),*

Otto-Ammann-Platz 9, 76131 Karlsruhe, Germany

³*Quantum Matter Institute, University of British Columbia, Vancouver BC V6T 1Z4, Canada*

Using molecular dynamics (MD) simulations of a generic model, we investigate heat propagation in bottle-brush polymers (BBP). An architecture is referred to as a BBP when a linear (backbone) polymer is grafted with the side chains of different length N_s and grafting density ρ_g , which control the bending stiffness of a backbone. Investigating κ -behavior in BBP is of particular interest due to two competing mechanics: increased backbone stiffness, via N_s and ρ_g , increases the thermal transport coefficient κ , while the presence of side chains provides additional pathways for heat leakage. We show how a delicate competition between these two effects controls κ . These results reveal that going from a weakly grafting ($\rho_g < 1$) to a highly grafting ($\rho_g \geq 1$) regime, κ changes non-monotonically that is independent of N_s . The effect of side chain mass on κ and heat flow in the BBP melts are also discussed.

Keywords: Thermal conductivity, Quasi 1D materials, Bottle-brush polymers, Molecular dynamics simulations, Scattering.

I. INTRODUCTION

Understanding the structure-property relationship in polymers is at the onset of many developments in designing advanced functional materials for suitable applications [1–6]. This is particularly because polymers are an important class of soft matter, where a delicate entropy-energy balance dictate their physical properties [1–3]. While the properties of most commonly known polymers are governed by weak van der Waals (vdW) interactions, the strength of which is of the order of $k_B T$ under ambient temperature $T = 300$ K and k_B being the Boltzmann constant, the recent interest has been devoted to bio-compatible hydrogen bonded (H-bond) polymers having a relatively stronger interaction strength of about 4–8 $k_B T$ [7–12].

The use of different polymeric materials ranges from commodity items [13–16], complex electronic packaging [8], thermoelectrics [17–19], organic solar cells [6, 20], and/or defense purposes [21, 22], where they are often exposed to a variety of environmental conditions. These include, but are not limited to, temperature T , pressure p , and solvent conditions. In this context, one of the most intriguing properties of amorphous polymers is their ability to conduct the heat current, as quantified by the thermal transport coefficient κ [1, 4, 5]. Here, $\kappa \propto cv_g \Lambda$ with c , v_g , and Λ being the heat capacity, the group velocity, and the mean free path, respectively. Note that v_g is related to the material stiffness. In an amorphous polymer, where an individual polymer chain follows random walk statistics [23–25]), $\Lambda \rightarrow 0$ and thus leads to a smaller κ . More specifically, most vdW-based systems usually have $\kappa \rightarrow 0.1 - 0.2$ W/Km [9] and can reach as high as 0.4

W/Km for H-bonded systems [8, 9].

Even when the bulk κ of amorphous polymers is rather small, at the monomer level they have different pathways for energy transfer, i.e., between two bonded monomers and between a monomer and its non-bonded neighbors. The energy transfer rate between two bonded monomers is over two orders of magnitude faster than between the non-bonded monomers [26–28]. This behavior is expected because κ is directly related to the material stiffness [29]. For example, a carbon-carbon (C-C) bond has an elastic modulus of $\simeq 250$ GPa [30], while the vdW and H-bonded systems have 1–5 GPa [9]. Note that we draw an analogy with a C-C bond because they constitute the backbone of most known commodity polymers.

The increased bonded energy transfer rates are shown to play a key role in increasing κ . Typical examples are the chain oriented systems of polymer fibers [31] and polymer brushes [32], attaining $\kappa \geq 100$ W/Km. Here, an extended chain configuration can be approximated as a quasi one-dimensional crystal due to the periodic arrangement of monomers and thus κ is dictated by the phonon propagation along the direction of orientation. Phonon scattering occurs when there is a kink along the chain backbone [33] and/or if there is an added pathway (such as a side chain) for heat leakage [34], thus leads to a significant reduction in κ .

Side chains are often added in a variety of important polymeric architectures to control their physical properties. A typical class of experimentally relevant systems is conjugated polymers, such as P3HT [6, 20] and super yellow [35]. The backbones of these systems are extremely stiff, hence they remain insoluble in most common solvents (due to the obvious entropic effects). Short alkane chains are then attached to the backbones to improve their solubility and thus improving solution processing. As a consequence, when these systems self-assemble for a device application, such as organic solar cell, alkane chains play a key role. For example, when a device is

*Electronic address: manjesh@iitk.ac.in

†Electronic address: debashish.mukherji@ubc.ca

used under the high T conditions, one grand challenge is to remove the excess heat for its better performance. Typically this is done via adding high κ fillers [20] that often compromise the basic properties of the bare background material. In this context, it is particularly important to understand the heat propagation in the bare samples and, if possible, to provide a microscopic picture for the tunability in κ .

Another interesting system is the “so called” bottle-brush polymers (BBP) [36, 37]. These are of potential interest because they have the potential to be used as one-dimensional organic nanocrystals [38], low friction materials [39], solvent-free and supersoft networks [40], have extraordinary elastic properties [40], and pressure-sensitive adhesives [41]. Another important feature of BBP is that their backbone stiffness, as measured in the unit of Kuhn length ℓ_k , can be tuned by changing the side chain length N_s and the grafting density ρ_g . Here, $\ell_k \propto N_s^\alpha$ with $\alpha \simeq 0.5 - 1.0$ for $N_s \leq 40$ [37]. One of the earliest studies also predicted $\alpha = 15/8$ in the asymptotic limit [42].

The discussions presented above clearly show that a better microscopic picture is needed that provides a possible route to tune κ in the branched systems via macromolecular engineering. In this context, to the best of our knowledge, simulation studies dealing with κ in such systems are rather limited, except for one case study using all-atom simulations of backbone polynorbornene (PNB) grafted with polystyrene (PS) side chains [43]. Motivated by this need, we investigate the influence of side chains on the κ -behavior in the branched polymers using a generic model. For this purpose, we simulate a model system consisting of a set of BBPs with varying N_s and ρ_g . We decouple various effects on κ and show how a delicate balance between different system parameters control κ in BBPs. We note in passing that since the significance of such brush-like polymers range over a wide variety of polymer chemistry and thus investigating them at the all-atom level has its obvious limitations. Therefore, a generic model is more suitable, where a broad range of polymers can be represented within one generic framework, while ignoring the specific chemical details that often only contribute to a mere numerical pre-factor.

The remainder of the paper is organized under the following sections: method and model used for this study, results and discussions, and finally the conclusions are drawn.

II. MATERIALS, MODEL, AND METHOD

In this study we investigate two systems: namely a set of tethered BBPs and a set of BBP melts. In both cases, a BBP consists of a backbone of length N_b grafted with the side chains of different N_s and ρ_g , where $\rho_g = N_g/\lambda$. N_g is the number of chains grafted per backbone monomer and λ is the monomer distance along the backbone for grafting.

A. The polymer model

A well known generic polymer model is used for the BBPs [44]. Within this model, individual monomers interact via 6–12 Lennard–Jones (LJ) potential within a cut-off radius r_c . Unless stated otherwise $r_c = 2^{1/6}\sigma$. The results are represented in the units of LJ energy ϵ , LJ distance σ , mass of the individual monomers m , and time $t_o = \sigma\sqrt{m/\epsilon}$. The numbers that are representative of hydrocarbons are $\epsilon = 30$ meV $\simeq 1k_B T$, $\sigma = 0.5$ nm, and pressure $p_o = 40$ MPa [44].

The bonded monomers interact with an additional finitely extensible nonlinear elastic (FENE) potential $u_{\text{FENE}}(r) = -0.5kR_o^2 \ln[1 - (r/R_o)^2]$, where $k = 30k_B T/\sigma^2$ and $R_o = 1.5\sigma$. The effective bond length in this model is $\ell_b \simeq 0.97\sigma$ [44].

Simulations are performed using the LAMMPS molecular dynamics package [45, 46]. The equations of motion are integrated using the velocity Verlet algorithm [47]. The Langevin thermostat is employed to impose $T = 1\epsilon/k_B$ with a damping coefficient $\gamma = 1.0t_o^{-1}$. Note that the simulations are performed in different steps and thus the specific details will be presented wherever appropriate.

1. Tethered bottle-brushes

The tethered BBPs consist of $N_b = 500$, $N_s = 2 - 20$ and $\rho_g = 1/256 - 4$. A typical simulation snapshot of a BBP is shown in Fig. 1(a). The system size details for the tethered chains are listed in the Supplementary Table S1. The chain configurations are generated by constraining the first (index 1) and the last (index 500) backbone monomers. These chains are first equilibrated under canonical simulation for a time $t = 10^5 t_o$ in their tethered positions. The time step is chosen as $\Delta t = 0.005 t_o$. The equilibrium side chain monomer density profiles $\rho(r)$ are shown in Figs. 1(b–d) for different ρ_g and N_s .

Periodic boundary conditions are employed in all three directions, however, the box size along the lateral directions (i.e., x & y directions) are taken as $2(d + r_c)$, where d is the distance from the backbone at which $\rho(r)$ drops to zero in Figs. 1(b–d). This choice avoids a monomer to see its periodic image due to their lateral fluctuations.

2. Bottle brush melts

For the melts, we have taken $N_b = 50$ with $N_s = 10$ and 20 and $\rho_g = 1/2$ and 1. The number of chains N_c in a melt is chosen such that the total number of particles in a simulation box remains around $N \simeq 2.56 \times 10^5$, see the Supplementary Table S2. Here, we have chosen a smaller value of N_b to ensure the reasonable sample equilibration, while avoiding the effects arising because of the chain entanglement. Note also that the specific N

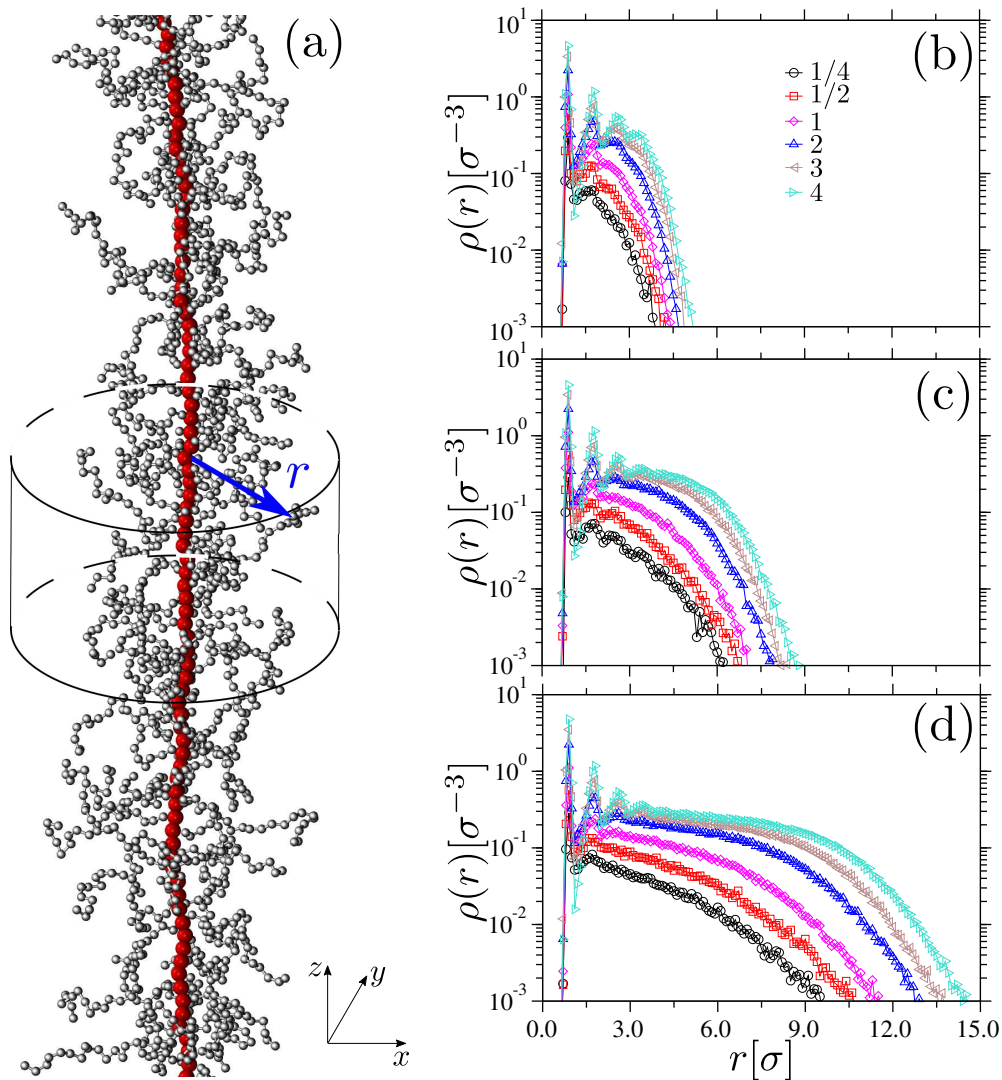


FIG. 1: Part (a) shows a representative simulation snapshot of a tethered bottle-brush polymer (BBP). This snapshot shows a section of a chain from the backbone length $N_b = 500$, a side chain length $N_s = 20$ and a grafting density $\rho_g = 1.0$, i.e., every backbone monomer is grafted with one side chain. The orientation of the chain is represented by the axis label in the right bottom corner. The thermal transport coefficient κ is calculated along the z -direction. The equilibrium monomer radial density profiles $\rho(r)$ are shown in parts (b–d). $\rho(r)$ is shown for the different ρ_g and for $N_s = 5$ (panel b), $N_s = 10$ (panel c), and $N_s = 20$ (panel d). Here, $\rho(r)$ is calculated in the cylindrical coordinate system, where the axis of a cylinder coincide with the orientation of the BBP backbone, and r is the radial distance from the backbone.

and $N_b = 50$ are chosen to be consistent with the system size taken in an earlier study of two of us in Ref. [48].

A melt configuration is generated by randomly placing N_c polymer chains in a cubic box at a monomer number density of $\rho_N \simeq 0.85\sigma^{-3}$ [44]. The melt samples are first equilibrated in the canonical ensemble for $t_{\text{equil}} \simeq 4 \times 10^6 t_o$ with $\Delta t = 0.01 t_o$. The corresponding mean-squared displacements $C(t)$ are shown in the Supplementary Fig. S1 and in the Supplementary Section S2. It can be appreciated that the total simulation time is at least an order of magnitude larger than the typical relaxation times of all BBPs and thus attaining well-equilibrated state, see the Supplementary Fig. S1.

For the κ calculations, we have imposed an attrac-

tive LJ interaction between the non-bonded monomers with $r_c = 2.5\sigma$. Here, two different values are chosen to mimic the monomer-monomer interactions between the side chains, namely $\epsilon_{ss} = 1.0\epsilon$ (referred as the default system, as in an earlier work [48]) and $\epsilon_{ss} = 1.2\epsilon$ (referred as the modified system). These systems are further equilibrated for $t_{\text{equil}} \simeq 4 \times 10^5 t_o$ with $\Delta t = 0.01 t_o$ under the canonical ensemble. These systems are then density equilibrated at a bulk pressure of $p = 0\epsilon/\sigma^3$ for $t_{\text{press}} \simeq 4 \times 10^5 t_o$ with $\Delta t = 0.01 t_o$. Pressure is imposed using the Nose-Hoover barostat [49, 50].

B. κ calculations

1. Non-equilibrium approach-to-equilibrium method

To calculate the thermal transport coefficient of full tethered chains κ_{full} , we have employed a non-equilibrium approach-to-equilibrium method [51]. Within this method, the length of a BBP L_z is divided into two parts along the direction of heat flow (see Fig. 1(a)). At the first step, 50 middle backbone monomers (including their side chains) are thermalized at $T_{\text{high}} = 4\epsilon/k_B$ and the remaining monomers are kept at $T_{\text{low}} = 0.67\epsilon/k_B$, which ensures that $\sum_{i=1}^{N_{\text{sc}}} T_i/N_{\text{sc}} = 1.0\epsilon/k_B$ and N_{sc} is the total number of particles in a tethered BBP. This thermalization is performed for a total time of $t_{\text{therm}} = 5 \times 10^5 t_o$ with a time step of $\Delta t = 0.005 t_o$. Subsequently, the thermostat is switched off and $\Delta T(t) = T_{\text{high}} - T_{\text{low}}$ is allowed to relax under microcanonical ensemble for $t_{\text{relax}} = 10^3 t_o$ with $\Delta t = 0.001 t_o$. Following Ref. [51], bi-exponential relaxation $\Delta T(t) = c_1 \exp(-t/\tau) + c_2 \exp(-t/\tau_z)$ is used to obtain the time constant of the energy flow along the z -direction τ_z . τ , c_1 and c_2 are the longitudinal energy transfer rate, and two constant pre-factors, respectively. κ_{full} is then calculated using,

$$\kappa_{\text{full}} = \frac{1}{4\pi^2} \frac{cL_z}{A\tau_z}. \quad (1)$$

Here, heat capacity is estimated using the classical Dulong-Petit limit $c = 3N_{\text{sc}}k_B$, $L_z = 499\ell_b$, and $A = \pi r^2$ is the cross-section area and the effective radius r is estimated from $\rho(r)$ in Fig. 1(b-d), i.e., when $\rho(r)$ drops to about 50% of its maximum value [32]. See the Supplementary Table S3 for more details.

2. Equilibrium Kubo-Green method

The Kubo-Green method [52], where κ is estimated using,

$$\kappa = \frac{v}{Dk_B T^2} \int_0^{\mathcal{T}} \langle \mathbf{J}(t) \cdot \mathbf{J}(0) \rangle dt. \quad (2)$$

The heat flux auto-correlation function $\langle \mathbf{J}(t) \cdot \mathbf{J}(0) \rangle$ is calculated in the microcanonical ensemble. Here, v is the system volume, D is the dimensionality, and \mathcal{T} is the range of integration that in our case is taken to be at least one order of magnitude larger than the typical de-correlation time. This method is used to calculate the backbone thermal transport coefficient κ_{BB} and for the melts κ_{melt} .

To calculate κ_{BB} we have used,

$$\kappa_{\text{BB}} = \frac{v_{\text{BB}}}{k_B T^2} \int_0^{\mathcal{T}_{\text{BB}}} \langle J_z(t) \cdot J_z(0) \rangle dt, \quad (3)$$

where volume of the backbone is estimated as $v_{\text{BB}} = \pi\sigma^3 N_b/6$ [32] and $\mathcal{T}_{\text{BB}} \simeq 100t_o$ with $\Delta t = 0.005t_o$. κ_{BB} is averaged over 20 independent runs.

For the calculation of thermal transport coefficient of the BBP melts κ_{melt} , we used have Eq. 2. In this case, $\mathcal{T} \simeq 100t_o$ with $\Delta t = 0.005t_o$ and κ_{melt} is average of five independent runs.

3. Some notes on the choice of methods for κ calculations

We have chosen two different methods for κ calculations because of their individual advantages. Furthermore, since both methods reproduce the same trends, we believe to be in the right method choices.

The non-equilibrium methods usually suffer from length effects, especially in the quasi one-dimensional systems, because of the boundary scattering and hence leads to a smaller estimates of κ that depend on L_z . Additionally, the approach-to-equilibrium is a relatively easy and computationally efficient method.

For the component-wise κ and also melts with relatively smaller system sizes, the Kubo-Green method may be more suitable because it produces κ equivalent to their values in the asymptotic limit. Here, however, the Kubo-Green method usually requires very careful sampling of the heat flux auto-correlation function and possible averaging over several independent runs.

All κ data presented here are normalized relative to the thermal transport coefficient of a linear chain (without the side chains) κ_{linear} . Here, we have used three estimates of κ_{linear} calculated for three different systems and two different methods. Fig. 2 uses $\kappa_{\text{linear}} = 141 \pm 17k_B/t_o\sigma$ calculated using Eq. 1. For Figs. 5 & 7, $\kappa_{\text{linear}} = 830 \pm 50k_B/t_o\sigma$ calculated using Eq. 3. For Fig. 8, we have used $\kappa_{\text{linear}} = 5.4 \pm 0.3k_B/t_o\sigma$ taken from an earlier work of two of us [48].

III. RESULTS AND DISCUSSIONS

A. Thermal conductivity of tethered chains

1. Full bottle-brushes

We begin by discussing the heat flow in full BBPs. In Fig. 2, we show $\kappa_{\text{full}}/\kappa_{\text{linear}}$ with changing N_s for two different ρ_g . Two distinct trends are clearly visible:

- κ_{full} decreases monotonically with increasing N_s for both ρ_g . This behavior is consistent with the trends observed in all-atom simulations of PNB grafted with PS [43], where a reasonable quantitative agreement is observed.
- κ_{full} decreases with increasing ρ_g , i.e., going from the red to the black data set in Fig. 2. This behavior is also consistent with the earlier results where

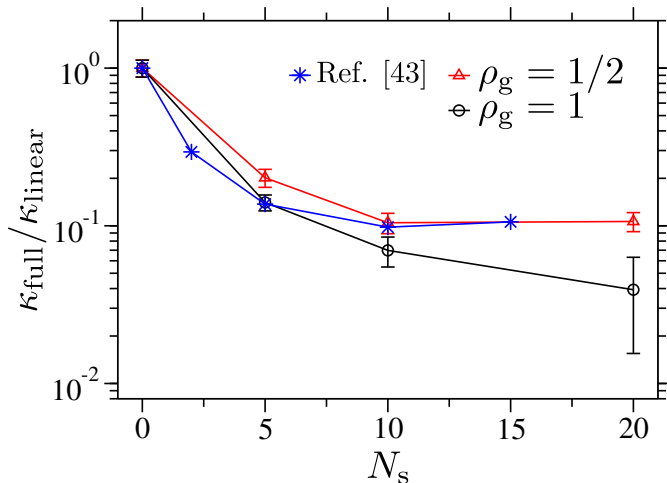


FIG. 2: The normalized thermal transport coefficient of the full chain $\kappa_{\text{full}}/\kappa_{\text{linear}}$ as a function of side chain length N_s for two different grafting densities ρ_g . κ_{full} is normalized with the thermal transport coefficient of a single linear polymer without the side chains $\kappa_{\text{linear}} = 141 \pm 17k_B/t_0\sigma$. The error bars are the standard deviation calculated from 20 independent simulation runs. For comparison, we have also included the all-atom reference data from Ref. [43].

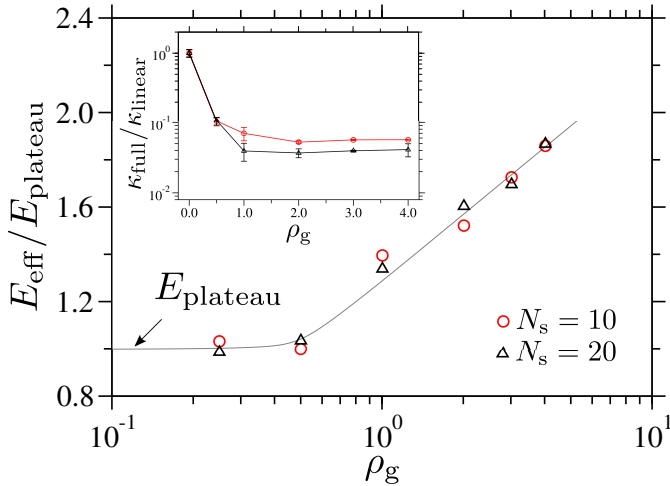


FIG. 3: The main panel shows the normalized effective bending stiffness of a bottle brush E_{eff} as a function of the grafting density ρ_g . The data is normalized with the plateau value $E_{\text{plateau}} = 6.7$ for $\rho_g \rightarrow 0$. Data is shown for two side chain lengths N_s . In the inset we show the normalized thermal transport coefficient of full chain $\kappa_{\text{full}}/\kappa_{\text{linear}}$ as a function of ρ_g .

κ_{full} was shown to decrease with increasing number of side chains along a backbone [34].

While the data in Fig. 2 show a nice correlation between the generic model and the corresponding all-atom data from the literature, we will now focus on a more fundamental understanding. In this context, κ_{full} is governed by a delicate combination of different contribu-

tions: the bonded interactions along the backbone chain, the non-bonded contacts between the side chains, and the heat leakage pathways due to the side chains. Here, a backbone chain consists of a periodic arrangement of monomers, where heat is carried by phonon propagation. When defects appear along the backbone, phonons scatter and thus reduce κ_{full} . In BBPs, the defects arise from: (a) the flexural vibrations of the backbones itself and (b) the heat leakage due to the grafted side chains.

As of part (a), it is known that the backbone of a BBP becomes stiffer with increasing N_s and/or by increasing ρ_g , as estimated by ℓ_k [36, 37]. The smaller the ℓ_k value, the greater the number of kinks N_{kink} along a backbone for a given N_b . A defect kink along the backbone scatters phonon. Indeed, it has been observed that increasing N_{kink} significantly reduces κ of an isolated chain [33] and of a chain in a polymer brush [32].

For a chain under the self-avoiding random walk configuration, ℓ_k can be estimated from the single chain structure factor [23, 24] or from the bond-bond auto-correlation function [37]. However, for our tethered chains, we have first calculated the effective flexural stiffness by using $E_{\text{eff}} \simeq F/\delta$, where F is the force required to keep the center monomer of a chain at a lateral displacement $\delta = 5\sigma$, see the Supplementary Section S3 and the Supplementary Fig. S2 for more details. In Fig. 3, we show the variation in E_{eff} with ρ_g . It can be appreciated that E_{eff} increases with increasing ρ_g , which is expected given that the effective diameter of a BBP increases with increasing ρ_g and the thicker cylinder give larger bending stiffness, see Figs. 1(b-d) and the Supplementary Table S3.

Even when the data in Fig. 3 reveal that the chains become stiffer with increasing ρ_g , κ_{full} shows a qualitatively different trend with ρ_g , see the inset in Fig. 3. This highlight that the heat flow in BBP is rather non-trivial and that the side chains play a more dominant role than just increasing the backbone flexural stiffness (scenario b, above). We will again come back to this at a later stage of this draft.

We note in passing that the flexural stiffness does not only increase with ρ_g , rather it should (ideally) also increase with N_s . Within the range of our choice of N_s , however, we do not observe any variation in E_{eff} with N_s , see the two data sets in the main panel of Fig. 3. This may be understood under two different conditions.

For the first condition, looking into $\rho(r)$ in Fig. 4, it can be appreciated that $\rho(r)$ remains rather constant up to a distance (highlighted by the vertical black lines, which we refer to as r^*) for both N_s and at a given ρ_g . Furthermore, we assume that E_{eff} is majorly governed by the core, while the top layer of the a brush only act as a soft surface that only contributes marginally to the total E_{eff} . Indeed, a previous study has shown that the stress on the top layers decreases rather rapidly (i.e., within a few particle diameters) [32]. In this study, we have also attempted to calculate stress in BBPs, which, however, suffered from a poor signal to noise ratio because of the

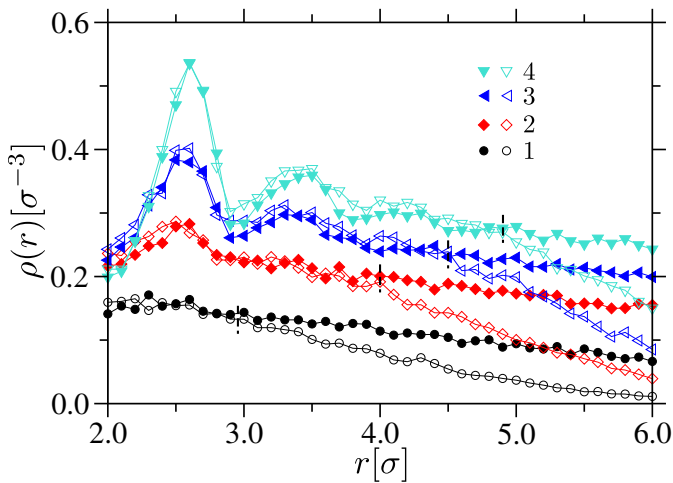


FIG. 4: Same as Figs. 1(c-d), however, only for the grafting density ρ_g within the range 1–4. The data for the side chain length $N_s = 10$ is shown by the empty symbols and the solid symbols are for $N_s = 20$. Vertical lines in every set correspond to the r values below which both N_s have the same $\rho(r)$.

short N_s , and thus we abstain from this calculation.

For the second condition, due to the short N_s values, chains also readjust upon lateral deformation and thus only contribute marginally to E_{eff} . We expect the effect of N_s to be more significant on E_{eff} in the case of longer side chains, especially for the grafting much larger than the critical grafting density for a N_s .

2. Only backbone of the bottle-brushes

In this section, we will now focus on the backbone contributions to κ_{full} . For this purpose, we show $\kappa_{\text{BB}}/\kappa_{\text{linear}}$ as a function of N_s in Fig. 5(a), where κ_{BB} is the thermal transport coefficient only for the backbone monomers without incorporating the side chains into the calculations. κ_{BB} also decreases with increasing N_s , a similar trend as κ_{full} shown in Fig. 2. A closer look at the data sets in Fig. 5(a) reveal a weak non-monotonic trend with increasing ρ_g for a given N_s . We have, therefore, re-plotted the data from Fig. 5(a) in Fig. 5(b), where the variation in κ_{BB} with ρ_g is shown. To investigate the extent of backbone stiffening due to grafting, we have included additional data when ρ_g is increased such that every monomer is grafted with more than one side chain. It can be appreciated that κ_{BB} indeed increases when $\rho_g \geq 1$ and thus highlight that the backbone stiffness is starting to contribute significantly to κ_{BB} , while the heat leakage by the side chains gets compensated to some degree.

Within the picture discussed above, we can now identify two distinct regimes: (I) For $\rho_g \leq 1/2$, E_{eff} remains rather constant and κ_{BB} is majorly influenced by the side chains. (II) For $\rho_g \geq 1$, the backbone stiffening is dominant that overcomes scattering due to the side chains.

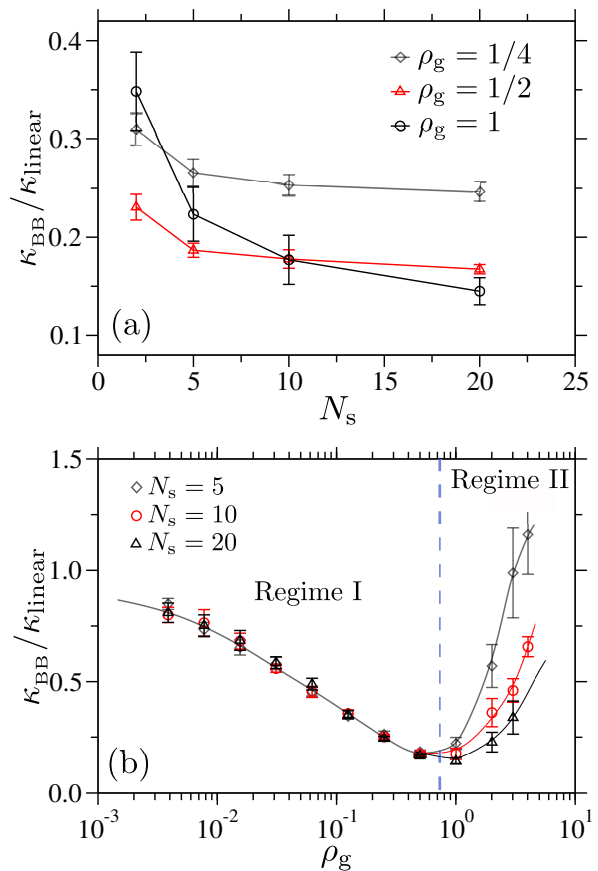


FIG. 5: Part (a) shows the normalized thermal transport coefficient $\kappa_{\text{BB}}/\kappa_{\text{linear}}$ for the backbone only (without incorporating the side chains in κ -calculations) as a function of side chain length N_s for different grafting densities ρ_g . Part (b) is a re-plot of the data in part (a) where $\kappa_{\text{BB}}/\kappa_{\text{linear}}$ is shown as a function of ρ_g for different N_s . The vertical dashed line gives an indication of the two regimes of the $\kappa_{\text{BB}}/\kappa_{\text{linear}}$ behavior. The error bars are the standard deviation calculated from 20 independent simulation runs. $\kappa_{\text{BB}}/\kappa_{\text{linear}}$ is normalized with the thermal transport coefficient of a single linear polymer without the side chains $\kappa_{\text{linear}} = 830 \pm 50 k_B/t_o\sigma$.

These two observed regimes also explain why κ_{full} first decreases rapidly for $\rho_g \leq 1$, while it remains rather constant for $\rho_g \geq 1$ (or even shows a weak signature of increase), see the inset in Fig. 3. This later behavior predominantly comes from an increased κ_{BB} and also because of the increased heat flow between the non-bonded contacts of the side chains for $\rho_g \geq 1$ (data not shown).

To illustrate the backbone stiffening and phonon scattering, we now calculate the vibrational density of states $g(\nu)$ with ν being the frequency. For this purpose, we first calculate the mass-weighted velocity autocorrelation function,

$$C(t) = \sum_i m_i \langle \vec{v}(t) \cdot \vec{v}(0) \rangle. \quad (4)$$

In Fig. 6(a) we show $C(t)/C(0)$ for a set of systems. The long lived fluctuations are clearly visible. Here, the global

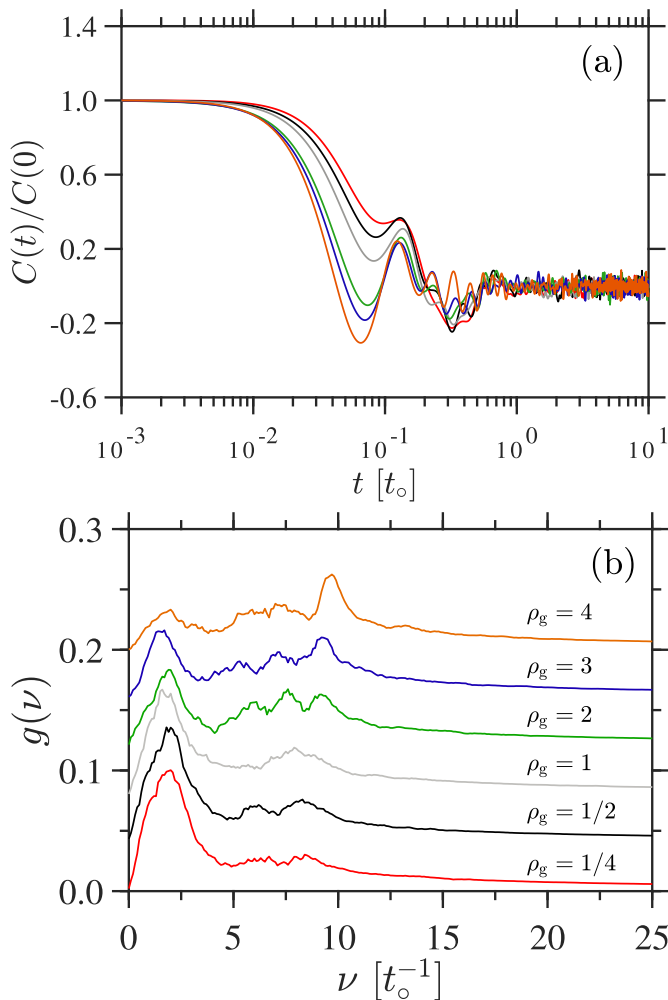


FIG. 6: Part (a) shows the normalized mass-weighted velocity autocorrelation function $C(t)$, which is calculated for the backbone monomers only by using Eq. 4. Part (b) shows the vibrational density of states $g(\nu)$ calculated using Eq. 5. The data is presented for different grafting density ρ_g and for a side chain length $N_s = 20$. For the clarity of presentation, individual $g(\nu)$ for different ρ_g are shifted by their additive y -offset. Colors are consistent between both panels.

$C(t)$ originate from the superposition of normal modes and thus its Fourier transform allows to compute $g(\nu)$ using [53, 54],

$$g(\nu) = \frac{1}{A} \int_0^\infty \cos(2\pi\nu t) \frac{C(t)}{C(0)} dt, \quad (5)$$

where the pre-factor A ensures $\int g(\nu) d\nu = 1$. Fig. 6(b) shows $g(\nu)$ for different ρ_g . A few distinct features are clearly visible:

- $g(\nu)$ shift towards higher ν with ρ_g . This shift is an indication of backbone stiffening with increasing ρ_g .
- The most prominent shift is observed for $\rho_g \geq 1$, which is also consistent the trend in Fig. 3. These

observations further show a nice correlation between increased stiffness and the observed apparent increase in κ_{BB} , see Fig. 5.

- The flexural vibrational peak around $\nu \simeq 7 - 10 t_0^{-1}$ (going from $\rho_g = 1/4 - 4$) becomes sharper with increasing ρ_g . In this context, it is known that the width of a peak in $g(\nu)$ is inversely proportional to the phonon life time [55], thus gives rise to a higher κ_{BB} .

In summary, the non-monotonic behavior in Fig. 5(b) is because of the two competing effects. The initial decrease in κ_{BB} for $\rho_g \rightarrow 1$ is dominated by the scattering via the presence of the side chain, where where the flexural stiffness remain rather invariant, see Figs. 3 & 6. The further increase in κ_{BB} for $\rho_{BB} \geq 1$ is because of the increased backbone stiffening that also leads to an increase in phonon life time. Note also that the peak around $\nu \simeq 2.5 t_0^{-1}$ comes from the non-bonded interactions.

3. Effect of side chain mass

It is noteworthy that the presence of side chains has a more complex influence in dictating the overall heat flow, i.e., N_s directly influences κ . Here, however, increasing N_s also implies that the backbones are grafted with the bulkier side chains. Therefore, it is rather practical to investigate: (1) What is the influence of the length N_s ? (2) What % of contribution comes directly from the increased the side chain mass? To this end, we start by showing the change in κ_{BB} with the side chain monomer mass m_s in Fig. 7. It can be appreciated that κ_{BB} decreases with increasing m_s , where the most dominant effect is observed for $\rho_g = 1$, see Fig. 7(c). This behavior is not surprising given that heat flow is directly proportional to the local vibrational frequencies and thus reduces with increasing m_s at a given T .

To identify the exact contribution due to the increased m_s , we have compiled Table I. Here, we show the percentage change in κ_{BB} by keeping the total mass $N_s m_s$ of the individual side chains constant, but having different N_s . It can be appreciated that the increased m_s always has an additional contribution in knocking down κ_{BB} . For example, κ_{BB} changes by an additional 10–13% for $m_s \leq 2$, while this effect is only about a few % for $m_s > 2$. This is a direct consequence of the behavior in Fig. 7, where a rapid decrease in κ_{BB} is observed for the smaller m_s and a weaker variation at higher m_s . We, however, can not state why exactly there is a significant difference between the two regimes, except the fact that mass seemingly always has a greater effect on the heat flow than the exact N_s .

We also want to briefly discuss a possible experimental system that could mimic the effect of mass difference, while keeping N_s fixed. For example, when the short alkane chains are added as the side groups, such as in the case of the conjugated polymers [6], they may be

TABLE I: A table listing the percentage change in the thermal transport coefficient of the backbone κ_{BB} for side chains with the same total mass but different side chain length N_s . The data is compiled for three different grafting densities ρ_g . The percentage difference is calculated with respect to the smaller κ_{BB} values. Here, m_s mass of the individual side chain monomer. κ_{BB} is normalized by the thermal transport coefficient of a linear tethered chain $\kappa_{\text{linear}} = 830 \pm 50k_B/t_o\sigma$.

N_s	m_s [m]	$\rho_g = 1/4$		$\rho_g = 1/2$		$\rho_g = 1$	
		$\kappa_{\text{BB}}/\kappa_{\text{linear}}$	Change[%]	$\kappa_{\text{BB}}/\kappa_{\text{linear}}$	Change[%]	$\kappa_{\text{BB}}/\kappa_{\text{linear}}$	Change[%]
10	1	0.253 ± 0.011	10.75	0.178 ± 0.009	12.80	0.177 ± 0.025	4.79
5	2	0.229 ± 0.011		0.158 ± 0.006		0.169 ± 0.015	
20	1	0.246 ± 0.010	10.50	0.167 ± 0.005	10.03	0.145 ± 0.014	10.26
10	2	0.223 ± 0.010		0.152 ± 0.005		0.131 ± 0.014	
10	2	0.223 ± 0.010	2.20	0.152 ± 0.005	0.91	0.131 ± 0.014	0.86
5	4	0.218 ± 0.011		0.151 ± 0.005		0.133 ± 0.012	
20	2	0.220 ± 0.011	4.46	0.149 ± 0.004	2.48	0.120 ± 0.007	1.12
10	4	0.211 ± 0.008		0.145 ± 0.008		0.119 ± 0.009	

replaced with polytetrafluoroethylene (PTFE). Note that one central difference between an alkane and a PTFE is that the hydrogen atoms are replaced with fluorines, hence effectively increasing the mass of a monomer by over a factor of three.

B. Thermal conductivity of bottle brush melts

Lastly, we would like to briefly discuss heat flow in BBP melt. In Fig. 8, we show the thermal transport coefficient of BBP melts κ_{melt} as a function of bulk modulus K , which is calculated using the volume fluctuation $K = k_B T \langle v \rangle / [\langle v^2 \rangle - \langle v \rangle^2]$. It can be appreciated that the systems with the default interaction (black data set in Fig. 8) have the same heat flow as the linear chain melt, i.e., $\kappa_{\text{melt}} \simeq \kappa_{\text{linear}}$, which is independent of the exact BBP architecture and N_s . This is, however, not surprising given that κ in melts, consisting of flexible polymers, is predominantly dictated by the non-bonded interactions [9, 48]. Only when the interaction between the side chain monomers is increased (see the red data set in Fig. 8) can one observe an increase in K and thus κ_{melt} . In this context, it is important to highlight that there exists peptide-based BBP [10] where side chains can have significantly larger interaction strengths, which may serve as a possible candidate in designing “smart” commodity plastics with improved thermal properties.

IV. CONCLUSIONS

We have presented a molecular dynamics study of heat flow in tethered bottle-brush polymers (BBP) and BBP melts, as quantified by the thermal transport coefficient κ . Our results show how the system parameters, such as the grafted side chain length N_s and their density ρ_g , control κ of the tethered BBP. In particular, we identify two different regimes in ρ_g : for $\rho_g < 1$ (weakly grafting regimes) scattering due to the side chains dominate κ , while the backbone stiffening plays a dominant when $\rho_g \geq 1$ (highly grafting regime). Polymer architecture does not play a significant role in dictating κ in BBP melts, where the interactions between the side chains are a dominant factor in controlling κ . As a broader perspective, our results establishes a structure-property relationship that may provide a guiding tool in designing advanced soft materials with improved thermal properties.

Supporting Information: This file contains additional data presenting the details of system sizes, the cross-section of BBPs, the equilibration of BBP melts, and the stiffness calculations.

Acknowledgement: M.K.M. and M.K.S. thank National Supercomputing Mission (NSM) facility PARAM Sanganak at IIT Kanpur where most of the single-chain simulations were performed. M.K.S. also thanks funding support provided by IIT Kanpur under initiation grant scheme. D.M. thanks the ARC Sockeye facility where some of these simulations are performed. For D.M. this

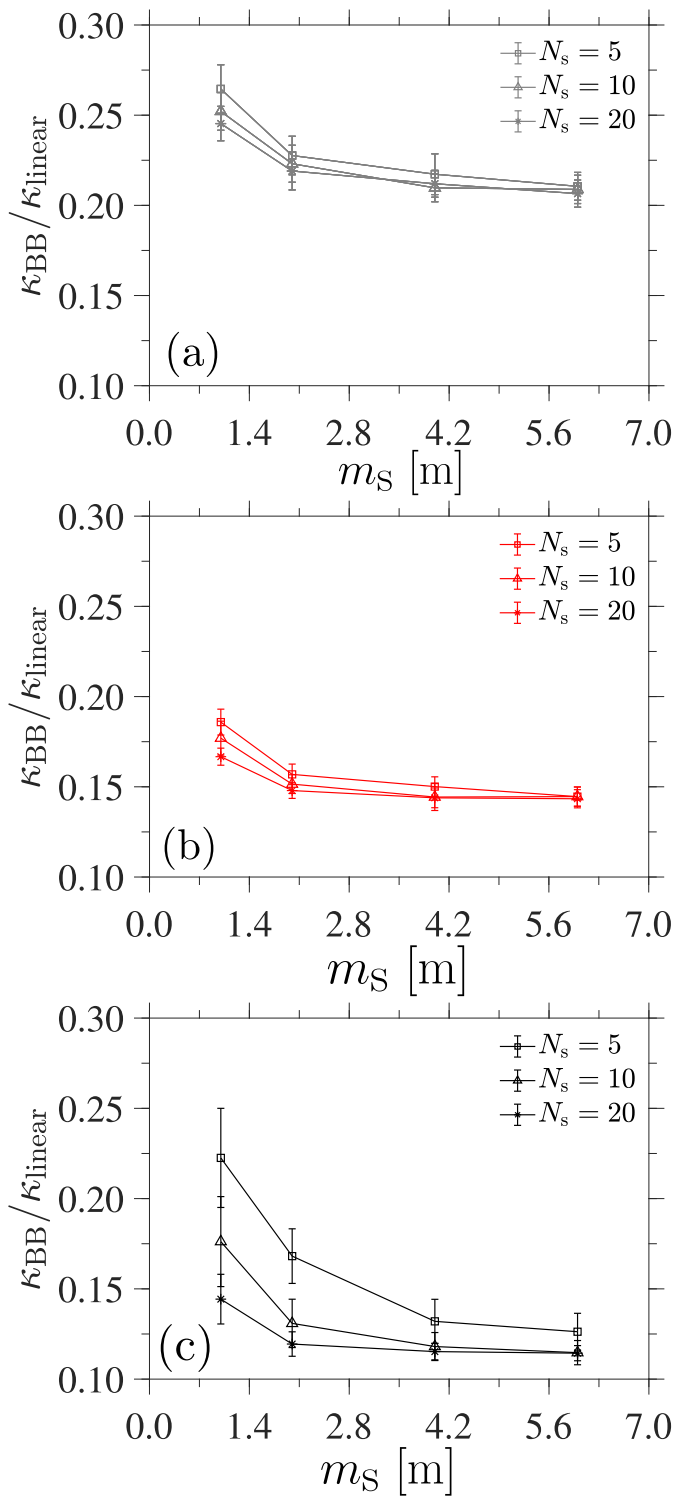


FIG. 7: Same as Fig. 5(a), however, as a function of monomer mass m_s of the side chains. The data is shown for three different side chain lengths N_s and two different grafting densities ρ_g . Parts (a–c) correspond to $\rho_g = 1/4, 1/2,$ and 1 , respectively.

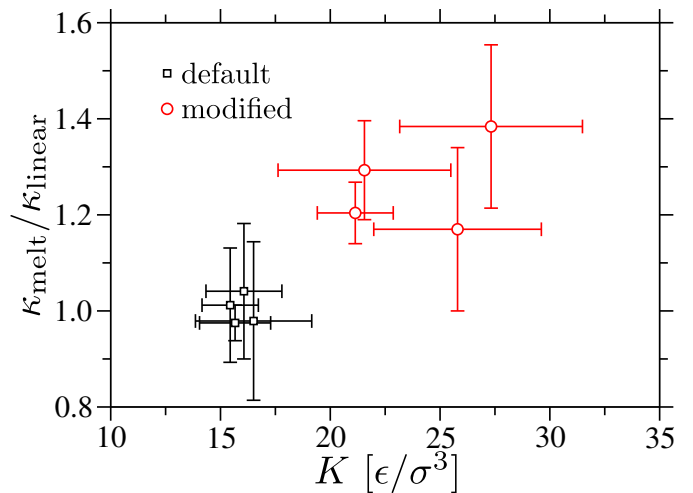


FIG. 8: The normalized thermal transport coefficient of bottle-brush polymer melt $\kappa_{\text{melt}}/\kappa_{\text{linear}}$ as a function of the bulk modulus K . The data is shown for two different interaction parameters between the monomers of the side chains, i.e., $\epsilon_{\text{ss}} = 1.0\epsilon$ (default system) and $\epsilon_{\text{ss}} = 1.2\epsilon$ (modified system). All other non-bonded monomer–monomer interaction is the same as the default system parameter. The thermal conductivity of the linear chain melt $\kappa_{\text{linear}} = 5.4 \pm 0.3k_{\text{B}}/t_{\text{c}}\sigma$ [48]. The error bars are the standard deviation calculated from five independent simulation runs.

research was undertaken thanks, in part, to the Canada First Research Excellence Fund (CFREF), Quantum Materials and Future Technologies Program.

Data availability: The scripts and the data associated with this research are available upon reasonable request from the corresponding author(s).

Competing interests: The authors declare no competing interests.

[1] A. Henry, “Thermal transport in polymers,” *Annu. Rev. Heat Trans.*, vol. 17, pp. 485–520, 2014.

[2] M. Müller, “Process-directed self-assembly of copoly-

- mers: Results of and challenges for simulation studies,” *Prog. Polym. Sci.*, vol. 101, p. 101198, 2020.
- [3] D. Mukherji, C. M. Marques, and K. Kremer, “Smart responsive polymers: Fundamentals and design principles,” *Annu. Rev. Cond. Mat.*, vol. 11, pp. 271–299, 2020.
 - [4] P. Keblinski, “Modeling of heat transport in polymers and their nanocomposites,” *Handbook of Mater. Model.*, pp. 975–997, 2020.
 - [5] X. Xu, J. Zhou, and J. Chen, “Thermal transport in conductive polymer-based materials,” *Adv. Funct. Mater.*, vol. 30, no. 8, p. 1904704, 2020.
 - [6] N. C. Forero-Martinez, K.-H. Lin, K. Kremer, and D. Andrienko, “Virtual screening for organic solar cells and light emitting diodes,” *Adv. Sci.*, vol. 9, no. 19, p. 2200825, 2022.
 - [7] G. R. Desiraju, “Hydrogen bridges in crystal engineering: interactions without borders,” *Acc. Chem. Res.*, vol. 35, no. 7, pp. 565–573, 2002.
 - [8] G. Kim, D. Lee, A. Shanker, L. Shao, M. S. Kwon, Gidley, J. Kim, and K. P. Pipe *Nat. Mater.*, vol. 14, pp. 295–300, 2015.
 - [9] X. Xie, D. Li, T. Tsai, J. Liu, P. V. Braun, and D. G. Cahill, “Thermal conductivity, heat capacity, and elastic constants of water-soluble polymers and polymer blends,” *Macromol.*, vol. 49, pp. 972–978, 2016.
 - [10] C. Chen, K. Wunderlich, D. Mukherji, K. Koynov, A. J. Heck, M. Raabe, M. Barz, G. Fytas, K. Kremer, D. Y. W. Ng, and T. Weil, “Precision anisotropic brush polymers by sequence controlled chemistry,” *J. Am. Chem. Soc.*, vol. 142, no. 3, pp. 1332–1340, 2020.
 - [11] D. Mukherji and K. Kremer, “Smart polymers for soft materials: from solution processing to organic solids,” *Polymers*, vol. 15, no. 15, p. 3229, 2023.
 - [12] B. Mendrek, N. Oleszko-Torbus, P. Teper, and A. Kowalczyk, “Towards next generation polymer surfaces: Nano- and microlayers of star macromolecules and their design for applications in biology and medicine,” *Prog. Polym. Sci.*, vol. 139, p. 101657, 2023.
 - [13] G. W. Halek, “Relationship between polymer structure and performance in food packaging applications,” *ACS Symp. Ser.*, vol. 365, pp. 195–202, 1988.
 - [14] J. Jain, W. Y. Ayen, A. J. Domb, and N. Kumar, *Chapter 1: Biodegradable polymers in drug delivery*. John Wiley & Sons, Inc. New York, 2011.
 - [15] G. Maier, “Polymers for microelectronics,” *Mater. Today*, vol. 4, no. 5, pp. 22–33, 2001.
 - [16] C. Ruscher, J. Rottler, C. E. Boott, M. J. MacLachlan, and D. Mukherji, “Elasticity and thermal transport of commodity plastics,” *Phys. Rev. Mater.*, vol. 3, p. 125604, 2019.
 - [17] W. Quirós-Solano, N. Gaio, C. Silvestri, G. Pandraud, and P. M. Sarro, “Pedot: Pss: a conductive and flexible polymer for sensor integration in organ-on-chip platforms,” *Procedia. Eng.*, vol. 168, pp. 1184–1187, 2016.
 - [18] W. Shi, Z. Shuai, and D. Wang, “Tuning thermal transport in chain-oriented conducting polymers for enhanced thermoelectric efficiency: a computational study,” *Adv. Funct. Mater.*, vol. 27, no. 40, p. 1702847, 2017.
 - [19] A. Tripathi, Y. Ko, M. Kim, Y. Lee, S. Lee, J. Park, Y.-W. Kwon, J. Kwak, and H. Y. Woo, “Optimization of thermoelectric properties of polymers by incorporating oligoethylene glycol side chains and sequential solution doping with preannealing treatment,” *Macromol.*, vol. 53, no. 16, pp. 7063–7072, 2020.
 - [20] M. K. Smith, V. Singh, K. Kalaitzidou, and B. A. Cola, “High thermal and electrical conductivity of template fabricated p3ht/mwcnt composite nanofibers,” *ACS Appl. Mater. Interfaces*, vol. 8, no. 23, pp. 14788–14794, 2016.
 - [21] I. M. McAninch, G. R. Palmese, J. L. Lenhart, and J. J. La Scala, “Characterization of epoxies cured with bimodal blends of polyetheramines,” *J. Appl. Polym. Sci.*, vol. 130, no. 3, pp. 1621–1631, 2013.
 - [22] R. M. Elder, D. B. Knorr, J. W. Andzelm, J. L. Lenhart, and T. W. Sirk, “Nanovoid formation and mechanics: a comparison of poly (dicyclopentadiene) and epoxy networks from molecular dynamics simulations,” *Soft Matter*, vol. 12, no. 19, pp. 4418–4434, 2016.
 - [23] J. D. Cloizeaux and G. Jannink, *Polymers in Solution: Their Modelling and Structure*. Clarendon Press, 1990.
 - [24] M. Doi and S. F. Edwards, *The Theory of Polymer Dynamics*. UK: Oxford Science Publications, 1986.
 - [25] P.-G. de Gennes, *Scaling Concepts in Polymer Physics*. Cornell University Press, 1979.
 - [26] S. Gottlieb, L. Pigard, Y. K. Ryu, M. Lorenzoni, L. Evangelio, M. Fernández-Regúlez, C. D. Rawlings, M. Spieser, F. Perez-Murano, M. Müller, and A. W. Knoll, “Thermal imaging of block copolymers with sub-10 nm resolution,” *ACS Nano*, vol. 15, no. 5, pp. 9005–9016, 2021.
 - [27] L. Pigard, D. Mukherji, J. Rottler, and M. Müller *Macromol.*, vol. 54, no. 23, pp. 10969–10983, 2021.
 - [28] J. Wu and D. Mukherji, “Comparison of all atom and united atom models for thermal transport calculations of amorphous polyethylene,” *Comput. Mater. Sci.*, vol. 211, p. 111539, 2022.
 - [29] D. G. Cahill, S. K. Watson, and R. O. Pohl, “Lower limit to the thermal conductivity of disordered crystals,” *Phys. Rev. B*, vol. 46, pp. 6131–6140, 1990.
 - [30] B. Crist and P. G. Hereña, “Molecular orbital studies of polyethylene deformation,” *J Polym Sci B Polym Phys*, vol. 34, no. 3, pp. 449–457, 1996.
 - [31] S. Shen, A. Henry, J. Tong, R. Zheng, and G. Chen, “Polyethylene nanofibres with very high thermal conductivities,” *Nat. Nanotechnol.*, vol. 5, no. 4, pp. 251–255, 2010.
 - [32] A. Bhardwaj, A. S. Phani, A. Nojeh, and D. Mukherji, “Thermal transport in molecular forests,” *ACS Nano*, vol. 15, no. 1, pp. 1826–1832, 2021.
 - [33] X. Duan, Z. Li, J. Liu, G. Chen, and X. Li, “Roles of kink on the thermal transport in single polyethylene chains,” *J. Appl. Phys.*, vol. 125, no. 16, p. 164303, 2019.
 - [34] C. Huang, X. Qian, and R. Yang, “Thermal conductivity of polymers and polymer nanocomposites,” *Mater. Sci. Eng. R Rep.*, vol. 132, pp. 1–22, 2018.
 - [35] S. Schliske, C. Rosenauer, T. Rödlmeier, K. Giringier, J. J. Michels, K. Kremer, U. Lemmer, S. Morsbach, K. C. Daoulas, and G. Hernandez-Sosa, “Ink formulation for printed organic electronics: Investigating effects of aggregation on structure and rheology of functional inks based on conjugated polymers in mixed solvents,” *Adv. Mater. Technol.*, vol. 6, no. 2, p. 2000335, 2021.
 - [36] J. Paturej, S. S. Sheiko, S. Panyukov, and M. Rubinstein, “Molecular structure of bottlebrush polymers in melts,” *Sci. Adv.*, vol. 2, no. 11, p. e1601478, 2016.
 - [37] P. E. Theodorakis, H.-P. Hsu, W. Paul, and K. Binder, “Computer simulation of bottle-brush polymers with flexible backbone: Good solvent versus theta solvent conditions,” *J. Chem. Phys.*, vol. 135, p. 164903, 10 2011.

- [38] X. Pang, Y. He, J. Jung, and Z. Lin, “1d nanocrystals with precisely controlled dimensions, compositions, and architectures,” *Science*, vol. 353, no. 6305, pp. 1268–1272, 2016.
- [39] X. Banquy, J. Burdyska, D. W. Lee, K. Matyjaszewski, and J. Israelachvili, “Bioinspired bottle-brush polymer exhibits low friction and amontons-like behavior,” *J. Am. Chem. Soc.*, vol. 136, no. 17, pp. 6199–6202, 2014.
- [40] W. F. Daniel, J. Burdyńska, M. Vatankhah-Varnoosfaderani, K. Matyjaszewski, J. Paturej, M. Rubinstein, A. V. Dobrynin, and S. S. Sheiko, “Solvent-free, supersoft and superelastic bottlebrush melts and networks,” *Nat. Mater.*, vol. 15, no. 2, pp. 183–189, 2016.
- [41] M. R. Maw, A. K. Tanas, E. Dashtimoghadam, E. A. Nikitina, D. A. Ivanov, A. V. Dobrynin, M. Vatankhah-Varnoosfaderani, and S. S. Sheiko, “Bottlebrush thermoplastic elastomers as hot-melt pressure-sensitive adhesives,” *ACS Appl. Mater. Interfaces*, vol. 15, no. 35, pp. 41870–41879, 2023.
- [42] C. M. Marques, *Les polymères aux interfaces*. PhD thesis, Éditeur inconnu, 1989.
- [43] H. Ma and Z. Tian, “Effects of polymer topology and morphology on thermal transport: A molecular dynamics study of bottlebrush polymers,” *Appl. Phys. Lett.*, vol. 110, no. 9, p. 091903, 2017.
- [44] K. Kremer and G. S. Grest *J. Chem. Phys.*, vol. 92, no. 8, pp. 5057–5086, 1990.
- [45] A. P. Thompson, H. M. Aktulga, R. Berger, D. S. Bolintineanu, W. M. Brown, P. S. Crozier, P. J. in ’t Veld, A. Kohlmeyer, S. G. Moore, T. D. Nguyen, R. Shan, M. J. Stevens, J. Tranchida, C. Trott, and S. J. Plimpton, “Lammps—a flexible simulation tool for particle-based materials modeling at the atomic, meso, and continuum scales,” *Comput. Phys. Commun.*, vol. 271, p. 108171, 2022.
- [46] S. Plimpton, “Fast parallel algorithms for short-range molecular dynamics,” *J. Comput. Phys.*, vol. 117, no. 1, pp. 1–19, 1995.
- [47] L. Verlet, “Computer” experiments” on classical fluids. i. thermodynamical properties of lennard-jones molecules,” *Phys. Rev.*, vol. 159, no. 1, p. 98, 1967.
- [48] D. Mukherji and M. K. Singh, “Tuning thermal transport in highly cross-linked polymers by bond-induced void engineering,” *Phys. Rev. Mater.*, vol. 5, p. 025602, Feb 2021.
- [49] G. J. Martyna, D. J. Tobias, and M. L. Klein, “Constant pressure molecular dynamics algorithms,” *J. Chem. Phys.*, vol. 101, no. 5, pp. 4177–4189, 1994.
- [50] B. Leimkuhler and C. Matthews, “Molecular dynamics,” *IJ. Interdiscip. Math.*, vol. 39, p. 443, 2015.
- [51] E. Lampin, P. L. Palla, P.-A. Francioso, and F. Cleri, “Thermal conductivity from approach-to-equilibrium molecular dynamics,” *J. Appl. Phys.*, vol. 114, no. 3, p. 033525, 2013.
- [52] R. Zwanzig, “Time-correlation functions and transport coefficients in statistical mechanics,” *Annu. Rev. Phys. Chem.*, vol. 16, no. 1, pp. 67–102, 1965.
- [53] J. Horbach, W. Kob, and K. Binder, “Specific heat of amorphous silica within the harmonic approximation,” *J. Phys. Chem. B*, vol. 103, pp. 4104–4108, May 1999.
- [54] H. Gao, T. P. W. Menzel, M. H. Müser, and D. Mukherji, “Comparing simulated specific heat of liquid polymers and oligomers to experiments,” *Phys. Rev. Mater.*, vol. 5, p. 065605, Jun 2021.
- [55] C. Kittel, *Introduction to Solid State Physics, Eight Edition*. John Wiley & Sons, 2005.

